Research
A SCIENCE PARTNER JOURNAL

RESEARCH ARTICLE

Synergistic Carbon Encapsulation and Silver Decoration Enable Durable and Selective CO_2-to-Ethylene Conversion on Copper Oxide Photoelectrode

Songying Qu[1], Ruiquan Yu[2], Min Gao[2], and Jun Zhang[3]*

[1]Macao Institute of Materials Science and Engineering, Faculty of Innovation Engineering, Macau University of Science and Technology, Taipa 999078, Macao SAR. [2]Institute of Environment and Ecology, Tsinghua Shenzhen International Graduate School, Tsinghua University, Shenzhen 518055, China. [3]Advanced Interdisciplinary Institute of Environment and Ecology, Guangdong Provincial Key Laboratory of Wastewater Information Analysis and Early Warning, School of Technology for Sustainability, Beijing Normal University, Zhuhai 519087, China.

*Address correspondence to: zhangboyu2016@163.com

Citation: Qu S, Yu R, Gao M, Zhang J. Synergistic Carbon Encapsulation and Silver Decoration Enable Durable and Selective CO_2-to-Ethylene Conversion on Copper Oxide Photoelectrode. *Research* 2026;9:Article 1206. https://doi.org/10.34133/research.1206

Submitted 18 December 2025
Revised 12 February 2026
Accepted 28 February 2026
Published 16 March 2026

Copyright © 2026 Songying Qu et al. Exclusive licensee Science and Technology Review Publishing House. No claim to original U.S. Government Works. Distributed under a Creative Commons Attribution License (CC BY 4.0).

Chemical alterations in metal oxides during manipulation greatly diminish their potential in artificial photosynthesis. Clarifying and overcoming these changes is crucial for realizing the sustainable generation of solar fuels and chemicals. Here, employing multimodal operando techniques, we elucidated the degradation mechanism of copper oxide (CuO_x) photocathodes under operational conditions, revealing an electron-mediated reductive photocorrosion pathway: $Cu_2O/CuO \rightarrow Cu_2O \rightarrow Cu$. These key findings led us to engineer an ultrathin carbon layer encapsulation strategy formed via electrodeposition-coupled self-assembly of carbon nanodots. This protective layer enables efficient photoelectron extraction and spatial isolation. The resulting CuO_x@C exhibits gratifying durability with unaltered phases and steady photocurrent throughout extended operation exceeding 24 h. To enhance activity and selectivity toward ethylene, Ag nanoparticles were integrated onto CuO_x@C. The Ag decoration enhances CO_2 adsorption, stabilizes *CO intermediate, and facilitates the crucial *CO–*CO coupling. The Faraday efficiency for CO_2-to-ethylene conversion on CuO_x@C/Ag reaches up to ~66.4% and retains ~95% of its initial performance after prolonged use. This synergistic strategy of carbon encapsulation and metal decoration exhibits broad applicability, as validated by CuO_x@C/Ru, CuO_x@C/Pd, and $BiVO_4$@C/Pt. Our work provides a universal design framework for efficient and durable photoelectrodes, accelerating their transition from laboratory prototypes to scalable technologies.

Introduction

The consumption and combustion of fossil fuels have caused severe energy shortages and environmental pollution, posing a major challenge to sustainable development [1,2]. To address it, there is increasing focus on the conversion and storage of renewable solar energy, especially through the reduction of CO_2 into clean fuels as alternatives to fossil fuels [3,4]. Photoelectrochemical platforms, which utilize semiconductor photoelectrodes to absorb solar energy and drive uphill chemical reactions, offer a promising solution [5,6]. Among various photoelectrocatalysts, metal oxide photoelectrodes stand out owing to their low cost, facile preparation, and being environment friendly, which are crucial for practical applications [7,8].

However, existing efficient metal oxide photoelectrodes often suffer from catastrophic degradation under operational conditions, markedly hindering the development of photoelectrochemical systems as a viable alternative for energy conversion and storage [9,10]. Take, for example, copper oxide (CuO_x, a heterojunction of Cu_2O/CuO) photocathodes, possessing a narrow band gap as well as a suitable band alignment, which can effectively harvest sunlight to drive CO_2 reduction, hydrogen evolution, and nitrogen fixation, among others [11–13]. Unfortunately, CuO_x typically exhibits a sharp decay in activity and selectivity within a few minutes [4,14]. Despite the development of some schemes [15–17], up to now, the comprehension of the dynamic chemical transformations occurring in these materials, including CuO_x, under light exposure remains extremely limited, despite being crucial for determining how to precisely improve their stability [18,19]. In this context, a rigorous understanding of the chemical transformation pathways of unstable photoelectrodes including CuO_x under operational conditions is imperative for designing rational protection strategies.

The most effective and convenient approach to overcoming the activity–stability trade-off is to deposit a conformal on unstable photoelectrodes [20,21]. Ideally, such a surface layer

can promote carrier dynamics in addition to preventing degradation. However, the processes for constructing protective layers reported to date, such as the deposition of TiO_2, graphene, g-C_3N_4, metal-organic frameworks, and polypyrrole, are often complex, costly, nonuniform, and uncontrollable [22–26]. Moreover, the protective efficacy of these clad layers is generally mediocre and far from satisfactory. There is thus an urgent need for new surface coating materials and methods to advance the practical application of metal oxide photoelectrodes in artificial photosynthesis. While a protective layer can promote charge migration and separation, thus enhancing photostability, it fails to provide the precise active sites necessary for high activity and selectivity in specific catalytic transformations. To address it, we propose the strategic integration of tailored cocatalysts (e.g., Ag, Ru, and Pd) onto the protection layer, forming an innovative sandwich architecture [27–29]. This rational design strategy offers a versatile route toward efficient and durable photoelectrochemical systems.

Herein, we elucidated the photoelectrocatalytic transformation mechanisms of CuO_x, as a model photoelectrode, using a correlative characterization approach. Under illumination, CuO_x undergoes electron-mediated reduction photocorrosion, summarized as: $Cu_2O/CuO \rightarrow Cu_2O \rightarrow Cu$. To mitigate this degradation, we innovatively proposed an ultrathin carbon layer encapsulation strategy formed via the electrodeposition-coupled self-assembly of carbon nanodots (Fig. 1 and Fig. S1). This protective layer effectively extracts photoelectrons, thereby achieving spatial isolation. Further functionalization of the resulting CuO_x@C with Ag nanoparticles enhances the activity and selectivity of CO_2 reduction to ethylene (C_2H_4), achieving a Faraday efficiency (FE) of ~66.4% and retaining ~95% of its initial performance after prolonged use. This approach also stabilizes photoanodes (e.g., $BiVO_4$) extending their service life.

Results and Discussion

In situ visualization of CuO_x degradation

The degradation process and mechanism of CuO_x photoelectrodes were investigated using several in situ characterization methods. Scanning electron microscope (SEM) images showed that the pristine Cu base surface was smooth and clean, free of any impurities (Fig. 2A and Fig. S2). By contrast, the CuO_x surface became rough due to the formation of Cu_2O/CuO crystal (Fig. 2B). Irregularly shaped Cu_2O/CuO particles, with an average size of ~500 nm, were evenly embedded on the Cu base surface (Fig. 2C and Fig. S3). When CuO_x was subjected to 15 h of long-term photoelectrocatalytic CO_2 reduction operation, the photocurrent decayed severely and exhibited 3 distinct stages of change (Fig. 2D). In the first 2 h, the photocurrent dropped from ~−3.2 to ~−4.0 mA/cm^2 (Stage 1). Then, the photocurrent reversed and rose to ~−2.1 mA/cm^2 after the intermediate 10 h (Stage 2) and finally stabilized at ~−1.7 mA/cm^2 after the last 3 h (Stage 3). Meanwhile, copper ions continuously leached from CuO_x during the operation, and the leaching rate was slow at first, became fast, and went slow again, which corresponded to the photocurrent changes (Fig. S4). The cumulative amount of copper ions leached reached up to ~212 μg/L at the end of the reaction (Fig. 2E).

The fresh CuO_x was black in appearance but turned rufous after use, indicating an obvious change in morphology and structure (Fig. S5). SEM images showed that the used CuO_x surface became relatively flat, and the Cu_2O/CuO crystal particles became obscured in contour and amorphous, confirming the degradation of morphology and structure (Fig. 2F and G and Fig. S6). In situ Raman spectra indicated that the peaks of CuO declined heavily in Stage 1 and almost disappeared by the end (Fig. 2H). In contrast, the peaks of Cu_2O were markedly enhanced in Stage 1, and then gradually weakened until they became blurred. The results demonstrated the successive degradation of CuO and Cu_2O. X-ray diffraction (XRD) patterns further proved that the CuO phase had completely degraded in used CuO_x (Fig. 2I). Based on the x-ray photoelectron spectroscopy (XPS) of the Cu 2p spectrum of used CuO_x, the peaks of Cu^{2+} disappeared, while the peaks of Cu^+ were markedly enhanced (Fig. 2J). Meanwhile, the characteristic peaks of Cu^0 appeared in used CuO_x. XPS O 1s spectra showed that the peak corresponding to Cu–O bonds was severely reduced in used

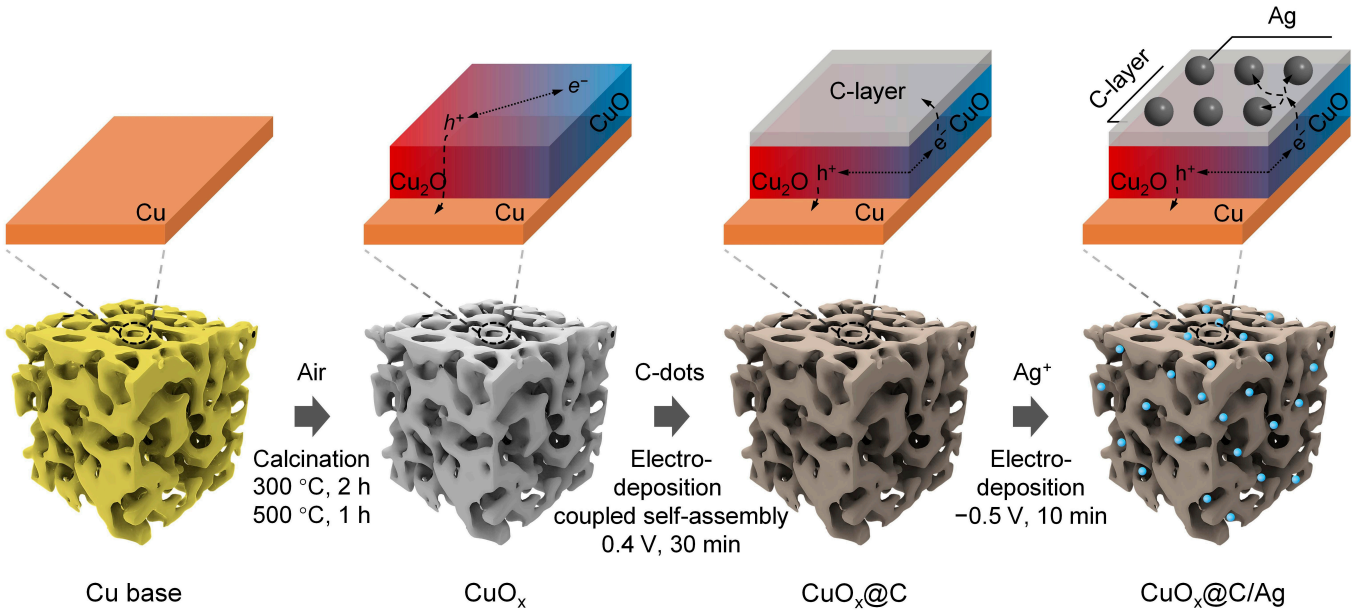


Fig. 1. Schematic diagram of synthesis path of CuO_x@C/Ag photoelectrodes.

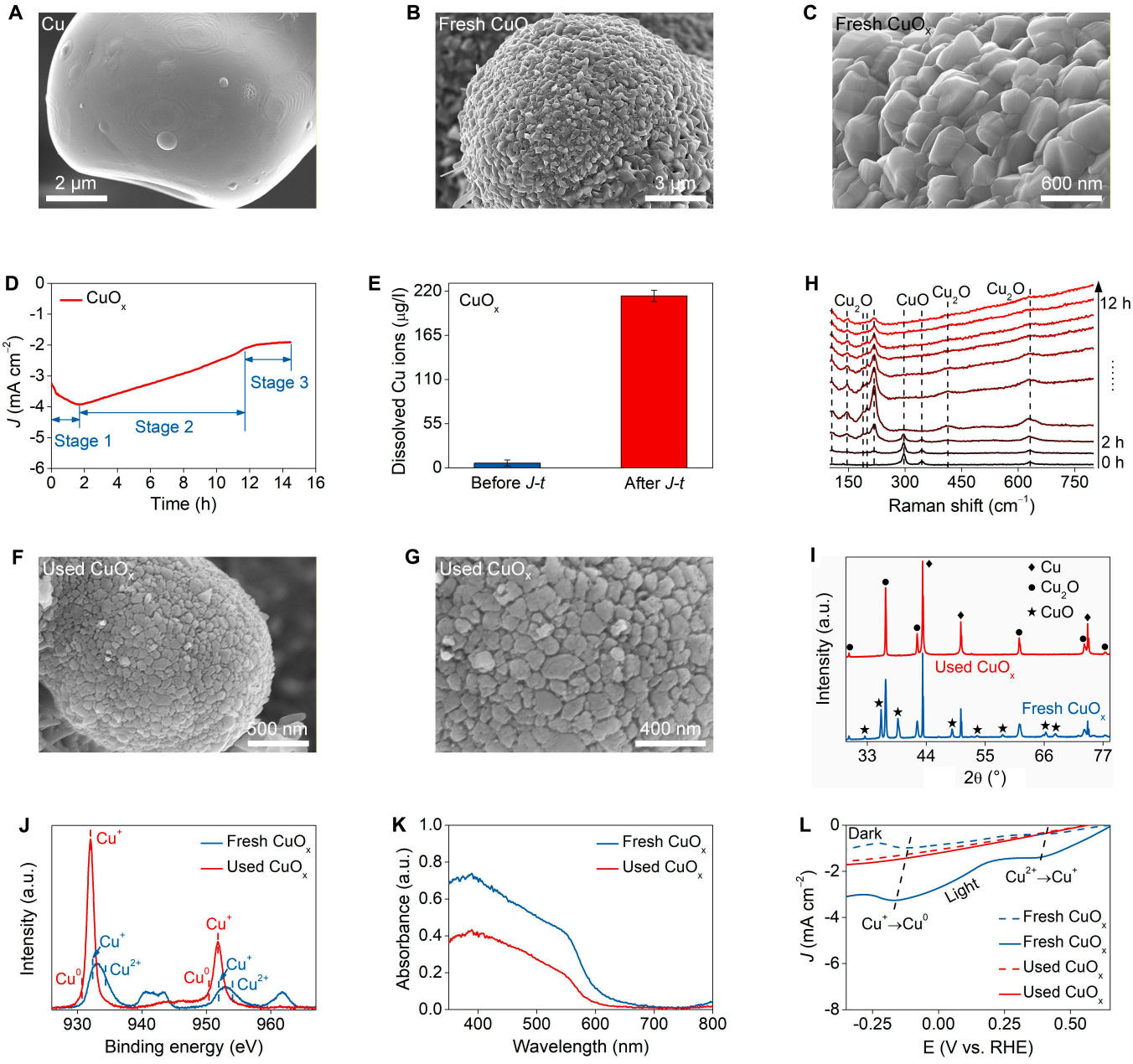


Fig. 2. In situ visual investigation of CuO_x degradation. The scanning electron microscope (SEM) images of (A) Cu base and (B and C) fresh CuO_x. (D) The *J*–*t* plot of CuO_x. (E) The released copper ions from CuO_x. (F and G) The SEM images of used CuO_x. (H) The in situ Raman spectra of CuO_x. The (I) x-ray diffraction (XRD) patterns, (J) x-ray photoelectron spectroscopy (XPS) spectra, (K) diffuse reflection spectroscopy (DRS) spectra, and (L) *J*–*V* plots of fresh and used CuO_x. Experimental conditions: at −0.1 V vs. reversible hydrogen electrode (RHE) under AM 1.5G simulated sunlight (100 mW/cm^2) using 0.1 M $KHCO_3$ as electrolyte (CO_2-saturated). Data are presented as mean ± SD ($n = 3$ independent chemical replicates) in (D).

CuO_x (Fig. S7). However, a new peak corresponding to Cu^{2+}–OH species appeared [4].

The above analyses revealed that most of the CuO phase in CuO_x was reduced to Cu_2O phase by photoelectrons in Stage 1, leading to a remarkable increase in the Cu_2O proportion (Fig. S8). The intrinsic activity of Cu_2O was better than that of CuO; thus, the absolute value of photocurrent increased slightly. This phase transition released a small amount of copper ions due to the loss of half of lattice oxygen. In Stage 2, most of Cu_2O sharply decayed to Cu, resulting in rapid photocurrent attenuation. This phase transition released a large amount of copper ions due to the loss of almost all lattice oxygen. In Stage 3, the remaining CuO and Cu_2O further degraded, resulting in continuous but gradual photocurrent reduction and copper ion release. The degradation process can be summarized as: Cu_2O/CuO → Cu_2O → Cu. Such electron-mediated severe photocorrosion led to an obvious decrease in the light capture performance and photoelectric conversion efficiency of used CuO_x (Fig. 2K and Fig. S9). Although the formation of Cu reduced the impedance and increased conductivity, the disappearance of active components resulted in disastrous photocurrent decay (Fig. 2L and Fig. S10).

In situ visualization of CuO_x@C durability

Next, we investigated the durability of CuO_x@C photoelectrodes using the same methods. SEM images showed that CuO_x was fully encapsulated in a carbon layer (Fig. 3A and B and Fig. S11). Transmission electron microscope (TEM) images illustrated that coating was extremely uniform, with an average thickness of ~6 nm, confirming that the carbon layer was formed by the self-assembly of single-row carbon nanodots (Fig. 3C and Figs. S12 and S13). When CuO_x@C was subjected to 15 h of long-term photoelectrocatalytic CO_2 reduction operation, the photocurrent remained almost constant (Fig. 3D). The absolute value of the photocurrent only decreased slightly from the initial ~4.8 mA/cm^2 to the final ~4.7 mA/cm^2. It is worth noting that the carbon layer encapsulation increased the onset photocurrent by ~30%. Additionally, there was extremely low copper ion leaching from CuO_x@C during the long-term operation, and the amount of copper ions leached did not exceed ~20 μg/L at the end of reaction (Fig. 3E and Fig. S14).

CuO_x@C was black in appearance, and its color hardly changed after use, indicating negligible changes in morphology and structure (Fig. S15). SEM and TEM images showed that used CuO_x@C surface was almost identical to fresh CuO_x@C, with the carbon layer (thickness ~6 nm) uniformly covering the CuO_x surface (Fig. 3F and G and Figs. S16 and S17). The atomic ratios of Cu, O, and C in CuO_x@C remained unchanged before and after use, further confirming the structural stability.

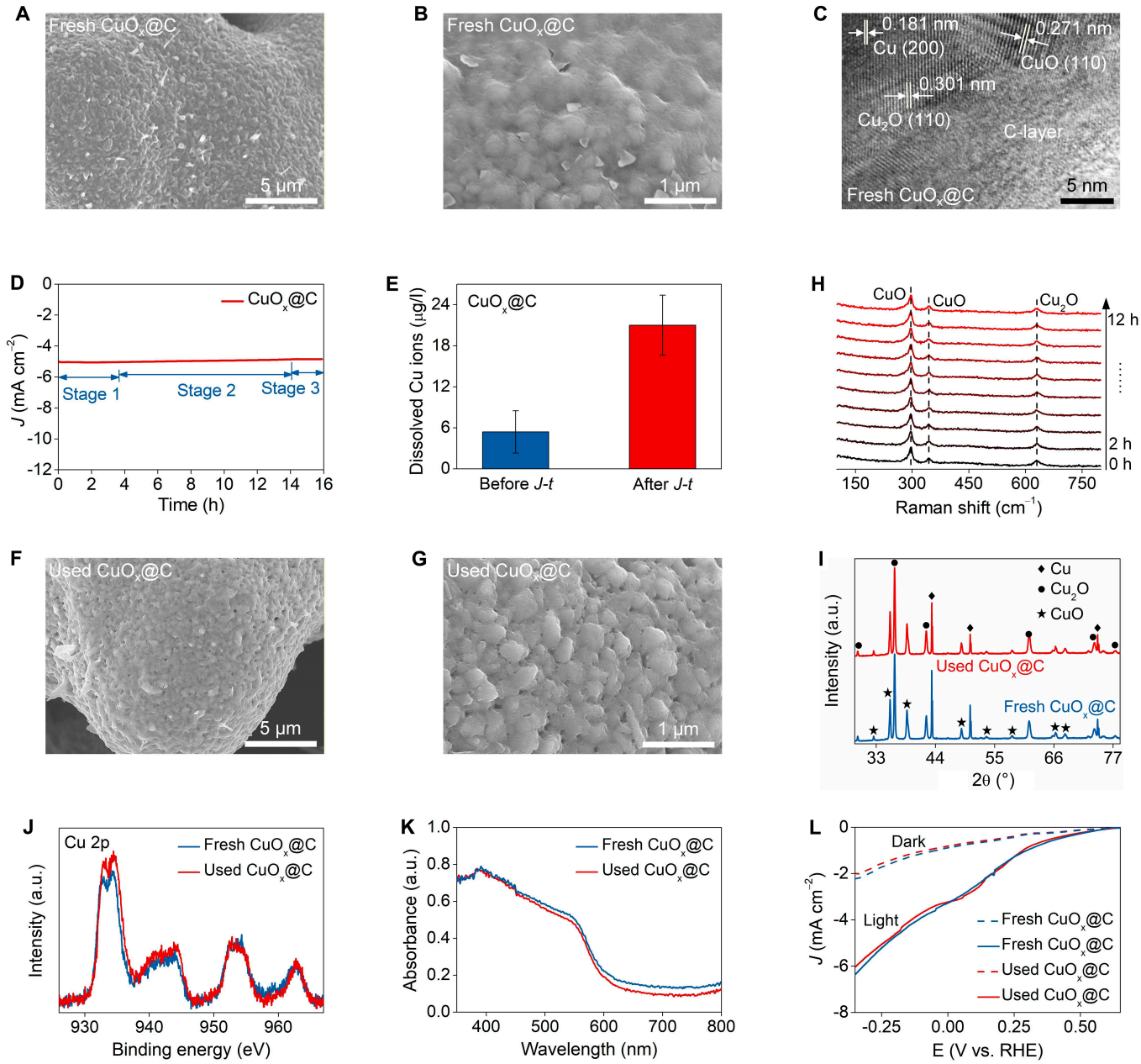


Fig. 3. In situ visual investigation of CuO_x@C durability. The (A and B) SEM and (C) transmission electron microscope (TEM) images of fresh CuO_x@C. (D) The *J*–*t* plot of CuO_x@C. (E) The released copper ions from CuO_x@C. (F and G) The SEM images of used CuO_x@C. (H) The in situ Raman spectra of CuO_x@C. The (I) XRD patterns, (J) XPS spectra, (K) DRS spectra, and (L) *J*–*V* plots of fresh and used CuO_x@C. Experimental conditions: at −0.1 V vs. RHE under AM 1.5G simulated sunlight (100 mW/cm^2) using 0.1 M $KHCO_3$ as electrolyte (CO_2-saturated). Data are presented as mean ± SD ($n = 3$ independent chemical replicates) in (D).

In situ Raman spectra indicated that the peaks of CuO and Cu_2O in CuO_x@C remained unchanged throughout the long-term operation (Fig. 3H and Fig. S18). XRD patterns further proved that neither CuO phase nor Cu_2O phase degraded during use (Fig. 3I). In the XPS spectra of Cu 2p, O 1s, and C 1s for CuO_x@C, the positions and intensities of all peaks remained largely unchanged before and after use (Fig. 3J and Figs. S19 and S20).

The above analyses revealed that the carbon layer encapsulation effectively mitigated CuO_x degradation, endowing CuO_x@C with gratifying durability. The CuO phase and Cu_2O phase remained stable throughout all stages of the long-term operation, resulting in a steady photocurrent with only slight attenuation (Fig. S21). Meanwhile, there was extremely low copper ion release due to the absence of obvious phase transition and lattice oxygen loss. This outstanding stability resulted in negligible changes in the light capture performance, photoelectric conversion efficiency, and electrochemical impedance of used CuO_x@C (Fig. 3K and Figs. S22 and S23). Linear sweep voltammetry (LSV) curves of CuO_x exhibited 2 reduction peaks, corresponding to the processes of $Cu^{2+} \rightarrow Cu^{1+}$ and $Cu^{1+} \rightarrow Cu^0$, respectively. In contrast, these 2 peaks were almost undetectable in the LSV curves of CuO_x@C, further demonstrating its satisfactory stability (Fig. 3L).

The protective mechanism of carbon layer encapsulation

The carbon layer acted as an electron reservoir and effectively extracted photoelectrons from CuO_x, resulting in spatial isolation and thus inhibiting photocorrosion (Fig. 4A and B). To accurately unveil the interfacial charge migration mechanism, the energy band structures of CuO_x, carbon layer, and CuO_x@C were systematically investigated (Fig. S24). Diffuse reflection spectroscopy (DRS) spectra revealed distinct optical absorption edges at ~605 nm for CuO_x and ~476 nm for carbon layer [30,31]. Tauc plots derived from the Kubelka–Munk transformation yielded an optical band gap (E_g) of ~2.06 eV for CuO_x and a molecular energy gap (ΔE) of ~2.60 eV for the carbon layer. Ultraviolet photoelectron spectroscopy (UPS) spectra positioned the valence band (VB) of CuO_x at ~−5.71 eV and the highest occupied molecular orbital (HOMO) of the carbon layer at ~−6.64 eV. The conduction band (CB) of CuO_x was derived as ~−3.65 eV (E_g + VB), and the lowest unoccupied molecular orbital (LUMO) of the carbon layer was found at ~−4.04 eV (ΔE + HOMO). These energy levels were calibrated relative to the reversible hydrogen electrode (RHE) scale using the standard conversion factor (−4.44 eV for 0 V) [32]. The resulting potentials positioned the CB and VB of CuO_x at ~−0.79 and ~1.27 V, respectively, while the LUMO and HOMO of carbon layer were located at ~−0.40 and ~2.20 V, respectively. CuO_x@C retained the precise band energy alignment of pristine CuO_x, indicating that a heterojunction was formed between CuO_x and the carbon layer.

Density functional theory (DFT) calculation was employed to simulate carrier dynamics [33,34]. Both CuO_x and the carbon layer had a relatively small work function (Φ), which facilitated smooth electron transfer from the bulk phase to the surface (Fig. 4C and D). The Fermi levels (E_F) of CuO_x and the carbon layer were −5.57 and −4.81 eV, respectively, indicating that the E_F of CuO_x was close to VB, while the E_F of the carbon layer was close to LUMO (Fig. 4E). When they came into contact with each other, electrons transferred from the carbon layer to CuO_x until an equilibrium state was reached, namely, the same E_F at interface. This created an internal electric field (IEF) that pointed from the carbon layer to CuO_x. Charge density difference and partial density of states (PDOS) further confirmed that there was obvious charge redistribution at the interface, with electrons accumulating around the CuO_x surface (Fig. 4F and Figs. S25 and S26). Meanwhile, the IEF bent the interfacial energy bands of CuO_x and the carbon layer, resulting in the formation of a Type II heterojunction between CuO_x and the carbon layer. During photoelectrocatalytic operation, photoelectrons continuously transferred from the CB of CuO_x to the LUMO of the carbon layer. Electron density distribution showed that the electrons mainly accumulated around oxygen atoms in CuO_x (Fig. 4G). By contrast, in CuO_x@C, electrons were extracted into carbon layer and evenly distributed around carbon atoms (Fig. 4H).

In situ Kelvin probe force microscopy (KPFM) was employed to map the spatial distribution of photocarriers in CuO_x@C (Fig. S27) [35–37]. The surface contact potential difference (CPD) of the carbon layer-coated edge zone and central CuO_x area was ~380 and ~420 mV, respectively. The CPD difference (ΔCPD) was up to ~40 mV, indicating that photoelectrons rapidly and directionally transferred from CuO_x to the carbon layer. Such fast charge migration and spatial isolation effectively suppressed electron–hole recombination and extended the photocarriers' lifetime, further evidenced by photoluminescence (PL) analyses. There was an obvious emission peak at ~364 nm in the steady-state PL spectrum of CuO_x, which was induced by the intrinsic radiative recombination in CuO_x (Fig. 4I). In contrast, the peak intensity dramatically decreased in CuO_x@C, implying the substantial inhibition of electron–hole recombination. Moreover, the recorded transient PL decay curves indicated that the average lifetime of carriers in CuO_x@C (~107.5 ns) was markedly longer than that in CuO_x (~67.1 ns) (Fig. 4J). Surface photovoltage (SPV) spectra showed that the SPV of CuO_x@C (~8.6 μV) was much smaller than that of CuO_x (~27.4 μV), further suggesting that electrons transferred and accumulated in the carbon layer in CuO_x@C (Fig. 4K). In short, the carbon layer effectively extracted photoelectrons from CuO_x, resulting in efficient inhibition of electron-induced reduction photocorrosion and suppression of electron–hole recombination, thereby enhancing the activity and durability of CuO_x@C (Fig. S28).

Rational design in selective catalytic conversion

The CuO_x photoelectrodes have garnered much attention in the fields of energy conversion and environmental purification, with applications including CO_2 reduction, nitrate reduction, and dehalogenation, among others [38–40]. To enhance the activity and selectivity of the target reactions, it was typically necessary to modify the CuO_x surface with specific cocatalysts, such as Ag, Ru, and Pd (Fig. 5A and Fig. S29) [28,29,41]. However, their wide application has been consistently hindered by the poor stability of CuO_x, which was caused by severe photocorrosion. In this work, we innovatively designed and synthesized the CuO_x@C photoelectrodes, which exhibited outstanding activity and unprecedented stability. As a result, CuO_x@C can replace conventional CuO_x and be further modified with specific cocatalysts, including Ag, Ru, and Pd, to achieve large-scale applications (Fig. S30).

We have successfully prepared ternary CuO_x@C/Ag hybrid by incorporating Ag onto the CuO_x@C through electrodeposition and used it for CO_2 reduction to C_2H_4 (Fig. 5B). SEM and EDX-mapping images revealed a uniform and dense distribution of Ag nanoparticles (~80 nm in diameter) firmly anchored

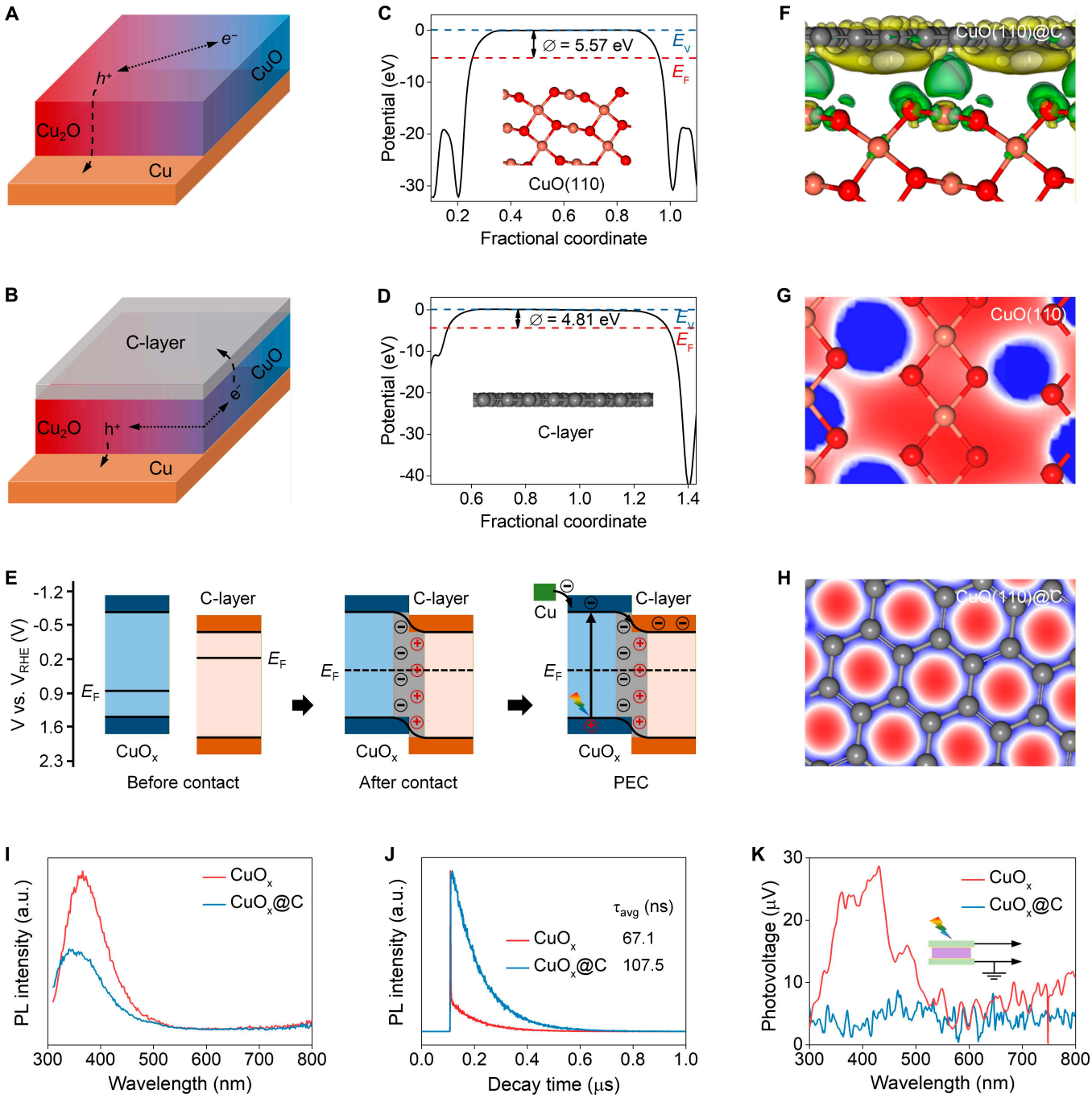


Fig. 4. The protective mechanism of carbon layer encapsulation. Schematic diagrams of migration and separation path of photogenerated carriers in (A) CuO_x and (B) CuO_x@C. Electrostatic potentials of (C) CuO(110) and (D) graphite carbon(100) (the yellow, red, and brown spheres stand for Cu, O, and C atoms; E_V denotes vacuum level). (E) Schematic illustration of CuO_x@C heterojunction: IEF-induced interfacial charge transfer, separation, and the formation of Type II heterojunction. (F) Side-view charge density difference map of CuO(110)/graphite carbon(100) (the yellow and green regions represent net electron accumulation and depletion). Electron density distribution of (G) CuO_x and (H) CuO_x@C (the blue and red regions represent net electron accumulation and depletion). The (I) steady-state PL spectra, (J) time-resolved transient PL spectra, and (K) SPV spectra of CuO_x and CuO_x@C. Experimental conditions: at −0.1 V vs. RHE under AM 1.5G simulated sunlight (100 mW/cm^2) using 0.1 M $KHCO_3$ as electrolyte (CO_2-saturated).

on the CuO_x@C surface in CuOx@C/Ag (Fig. 5C and Fig. S31). TEM image resolved distinct Ag (111) lattice fringes with a spacing of ~0.24 nm, confirming the excellent crystallinity of Ag nanoparticles, which was further corroborated by XRD patterns (Fig. S32) [41]. XPS spectra demonstrated that Ag nanoparticles remained predominantly in the metallic state both before and after prolonged photoelectrocatalytic CO_2 reduction operation, establishing metallic Ag^0 as the durable active phase in reaction, which was consistent with some previous reports (Fig. S33) [41,42]. DRS spectra showed that CuO_x@C/Ag exhibited markedly broadened and enhanced light absorption compared to CuO_x@C, which was mainly caused by the strong localized surface plasmon resonance of Ag nanoparticles (Fig. S34) [43]. KPFM measurements revealed a substantially enhanced ΔCPD (~60 mV) between edge zone and central area in CuO_x@C/Ag, indicating that the Ag modification further facilitated the

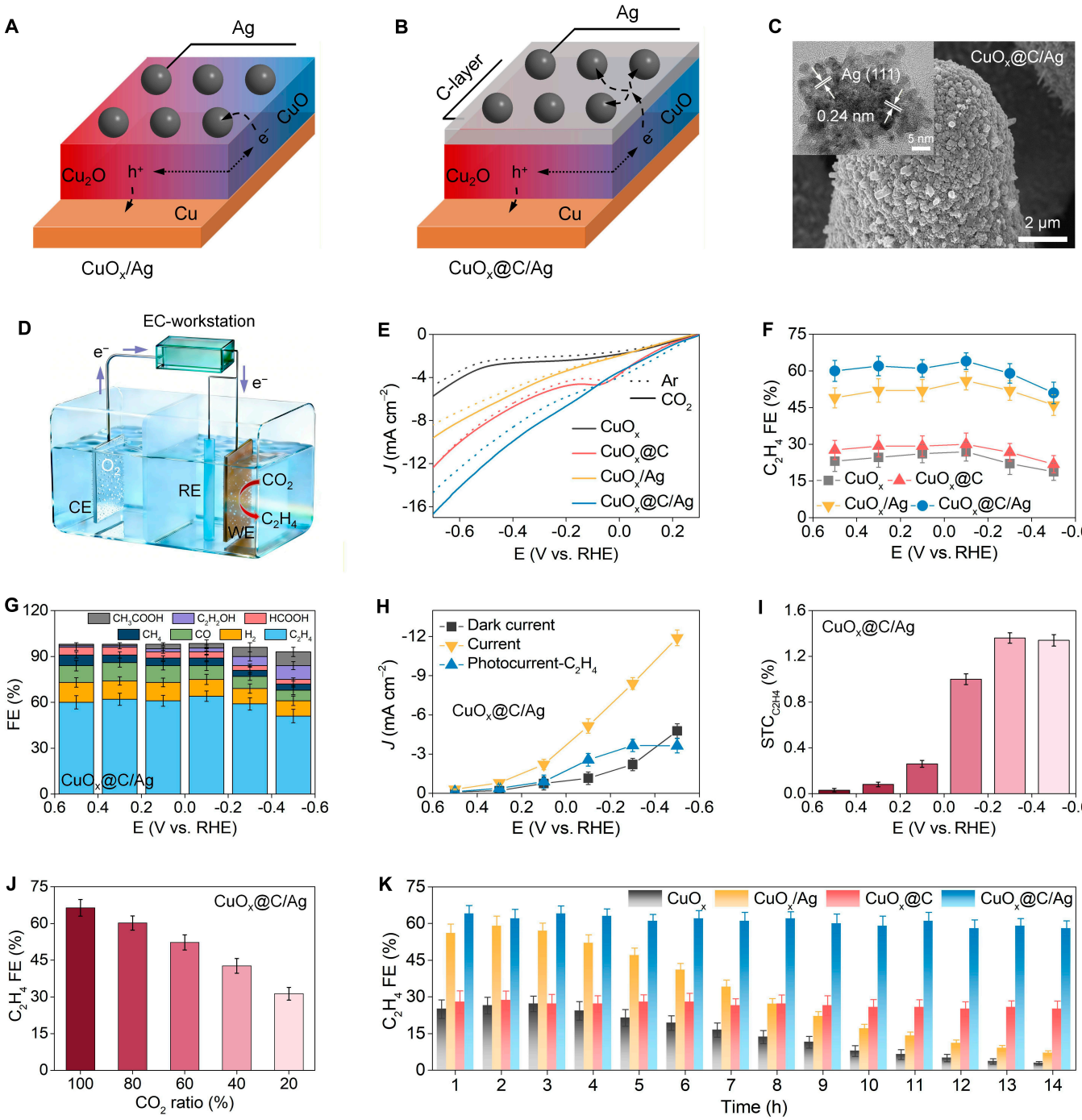


Fig. 5. Photoelectrocatalytic activity, selectivity, and stability for CO_2-to-C_2H_4 conversion. Schematic diagrams of migration and separation path of photogenerated carriers in (A) CuO_x/Ag and (B) CuO_x@C/Ag. (C) The SEM and TEM images of CuO_x@C/Ag. (D) The schematic diagram of photoelectrocatalytic CO_2 reduction. (E) The linear sweep voltammetry (LSV) curves of CuO_x, CuO_x@C, CuO_x/Ag, and CuO_x@C/Ag. (F) The C_2H_4 FE under different potentials on CuO_x, CuO_x@C, CuO_x/Ag, and CuO_x@C/Ag. (G) The FE of reduction products under different potentials on CuO_x@C/Ag. (H) The photocurrent density dedicated to C_2H_4 production under different potentials on CuO_x@C/Ag. (I) The STC conversion efficiency for C_2H_4 production under different potentials on CuO_x@C/Ag. (J) The C_2H_4 FE in different initial CO_2 concentrations on CuO_x@C/Ag. (K) The durability of CuO_x, CuO_x@C, CuO_x/Ag, and CuO_x@C/Ag for CO_2 reduction to C_2H_4. Experimental conditions: at −0.1 V vs. RHE under AM 1.5G simulated sunlight (100 mW/cm^2) using 0.1 M $KHCO_3$ as electrolyte (CO_2-saturated). Data are presented as mean ± SD ($n = 3$ independent chemical replicates) in (D).

charge migration and separation (Fig. S35). This was further validated by the PL spectra of CuO_x@C/Ag (Figs. S36 and S37). A substantially quenched steady-state PL emission at ~364 nm was observed, which was complemented by a markedly extended carrier lifetime of 126.4 ns in the transient PL decay. SPV spectra showed that the SPV value of CuO_x@C/Ag was as low as ~7.7 μV, indicating that the Ag nanoparticles served as electron sinks that effectively extracted electrons from the carbon layer (Fig. S38). The aggregation of electrons on the Ag surface was highly beneficial for subsequent CO_2 adsorption and activation. Electrochemical active surface area (ECSA) analysis indicates that carbon layer coating and Ag modification, the latter in

particular, markedly increase the ECSA, thereby offering more active sites available for the subsequent CO_2-to-ethylene reduction reaction (Fig. S39).

The photoelectrocatalytic activity, selectivity, and stability of CuO_x@C/Ag for CO_2 reduction to C_2H_4 was systematically evaluated (Fig. 5D). The CO_2 temperature-programmed desorption tests demonstrated that Ag decoration markedly enhanced CO_2 uptake, as evidenced by a distinct peak around 300 °C (Fig. S40). Such moderate-intensity adsorption not only facilitated efficient CO_2 activation but also promoted the timely desorption of products, thus preventing active-site blocking. LSV measurements showed that the modification with the carbon layer, Ag, and carbon layer/Ag increased the photocurrent density of CuO_x by ~2.1 times (CuO_x@C), ~1.7 times (CuO_x/Ag), and ~2.8 times (CuO_x@C/Ag), respectively, indicating greater electron accumulation on the CuO_x@C/Ag surface, which was conducive to enhancing the CO_2 reduction activity (Fig. 5E). Moreover, CuO_x/Ag and CuO_x@C/Ag exhibited a stronger response to CO_2 compared to CuO_x and CuO_x@C, demonstrating that Ag was a more effective active site for CO_2 activation. The C_2H_4 FE of CuO_x@C/Ag reached as high as ~66.4% at −0.1 V vs. RHE, obviously higher than that of CuO_x (~26.3%), CuO_x@C (~29.1%), and CuO_x/Ag (~54.7%), confirming the optimal selectivity of CuO_x@C/Ag for CO_2 reduction to C_2H_4 (Fig. 5F). The CuO_x@C/Ag maintained high C_2H_4 FE (>60%) across a wide potential window from 0.5 to −0.1 V vs. RHE, demonstrating its operational flexibility. At potentials below −0.1 V vs. RHE, the growing contribution of electrocatalysis promoted competing reduction channels, thereby leading to a moderate decline in C_2H_4 FE.

In addition to C_2H_4, some other products, including H_2, CO, CH_4, HCOOH, C_2H_5OH, and CH_3OOH, were also detected on CuO_x@C/Ag (Fig. 5G). Especially at low potentials, as the proportion of electrocatalysis increased, the FE of C_{2+} products markedly improved, which was consistent with the existing reports [44,45]. The effective photocurrent density of CuO_x@C/Ag dedicated to C_2H_4 production was derived by correcting the total current for dark contributions and scaling by the C_2H_4 FE (Fig. 5H). This value increased gradually as the potential decreases and then stabilized at potentials more negative than −0.3 V vs. RHE, reaching a maximum of ~−3.66 mA/cm^2, suggesting full extraction of available photogenerated carriers under these conditions. Correspondingly, the solar-to-chemical (STC) conversion efficiency for C_2H_4 production of CuO_x@C/Ag rose with decreasing potential before stabilizing, attaining a remarkable peak value of ~1.36% at −0.3 V vs. RHE (Fig. 5I). It was worth noting that even under a diluted CO_2 atmosphere (~20%), CuO_x@C/Ag retained a C_2H_4 FE exceeding 30%, highlighting its exceptional potential for practical deployment in real-world scenarios like industrial exhaust upgrading (Fig. 5J). Furthermore, the photoelectrocatalytic performance of CuO_x@C/Ag toward CO_2 reduction to ethylene was optimized by tuning the ratio of CuO to Cu_2O (Fig. S41). The results reveal that a CuO-to-Cu_2O ratio approaching 1:1 delivers the highest activity. This optimal performance is attributed to the formation of a more complete Type II heterostructure, which maximizes the density of Cu^{2+}–O–Cu^+ bond bridges, thereby facilitating the migration and separation of photogenerated charge carriers. The C_2H_4 FE of CuO_x and CuO_x/Ag sharply decreased from ~26.3% to ~2.9% and from ~54.7% to ~7.6%, respectively, after 14 h of continuous use (Fig. 5K). In contrast, CuO_x@C and CuO_x@C/Ag maintained >95% of their initial performance after prolonged operation. The accompanying time–current curves showed that CuO_x@C/Ag exhibited a remarkably stable current density with minimal decay, further underscoring its robust structural durability and resistance to deactivation (Fig. S42). Strikingly, the activity, selectivity, and durability of CuO_x@C/Ag for CO_2 reduction to C_2H_4 were outstanding and markedly superior to most existing studies (Fig. S43 and Table S1), demonstrating the effectiveness of the synergistic carbon encapsulation and Ag decoration strategy.

A comprehensive investigation of the reaction mechanism for CO_2 reduction to C_2H_4 on CuO_x@C/Ag was conducted. The $^{13}CO_2$ isotopic labeling experiment verified that the C_2H_4 production originated from CO_2 reduction rather than from other potential carbon sources (Fig. 6A). Meanwhile, the detection of ^{13}CO species definitively identified CO as a pivotal intermediate in the C_2H_4 formation pathway [46]. The differential electrochemical mass spectrometry (DEMS) results further revealed the simultaneous generation of substantial CO (m/z = 28) and C_2H_4 (m/z = 28, verified by its characteristic fragment C_2H_3 [m/z = 27]), confirming the conversion sequence of $CO_2 \rightarrow CO \rightarrow C_2H_4$ (Fig. 6B) [47]. The absence of DEMS signals of CH_4 (m/z = 16) and HCOOH (m/z = 46) further underscored the remarkable selectivity toward C_2H_4 production on CuO_x@C/Ag. The in situ attenuated total reflection Fourier-transform infrared (ATR-FTIR) spectroscopy collected on CuO_x@C/Ag showed that the distinct vibrational signatures of *CO (~2,053.1 cm^{-1}) and *COCHO (~1,112.2 and 1,637.3 cm^{-1}) were observed, while the characteristic *CHO band (~1,698.6 cm^{-1}) remained absent (Fig. 6C) [48,49]. This provided compelling evidence that the crucial C–C coupling step proceeded predominantly through symmetric dimerization of 2 *CO intermediates, rather than the alternative asymmetric *CO–*CHO pathway. The reaction cascade was reconstructed through further identification of additional intermediates, including *COOH (~1,216.2 and 1,480.3 cm^{-1}) and *$CHOCH_2$ (~1,567.2 cm^{-1}), collectively establishing the general reaction sequence of *$CO_2 \rightarrow$ *COOH $\rightarrow$ *CO $\rightarrow$ *COCO $\rightarrow$ *COCHO $\rightarrow$ *$CHOCH_2 \rightarrow$ *C_2H_4. In contrast, all these intermediate signals were markedly attenuated on the Ag-free CuO_x@C, consistent with its inferior activity and C_2H_4 selectivity, and highlighting the essential role of Ag in promoting intermediate stabilization and the decisive C–C coupling step (Fig. S44).

DFT calculations provided atomic-scale validation for the proposed reaction pathway (Fig. 6D and E and Fig. S45). The introduction of Ag markedly enhanced CO_2 adsorption, with adsorption energies strengthening from −0.25 eV (CuO_x@C) to −0.75 eV (CuO_x@C/Ag). The hydrogenation barriers of *CO_2 to *COOH dramatically reduced from 1.95 eV on CuO_x@C to 0.5 eV on CuO_x@C/Ag. This enhancement was further corroborated by differential charge density analysis, revealing substantial electron transfer between *CO_2 and CuO_x@C/Ag (Bader charge: 1.253 |e|) compared to only 0.744 |e| with CuO_x@C. The strengthened interaction facilitated C–O bond activation (from 1.171 to 1.183 Å) and enabled efficient *CO_2 hydrogenation. The resulting *CO intermediate was effectively stabilized on CuO_x@C/Ag, with adsorption energies of −0.3 eV, in contrast to positive values (0.4 eV) on CuO_x@C, where *CO tended to desorb. The comparison of formation barriers for *CO (−0.1 eV) and *HCOOH (0.1 eV) provided a theoretical foundation for the experimentally observed minimal HCOOH production. On CuO_x@C/Ag, the C–C coupling barrier via *CO dimerization (~0.7 eV) was markedly lower than the barrier for *CO hydrogenation to *CHO (~0.9 eV), establishing the thermodynamic preference for symmetric *CO dimerization over asymmetric *CO–*CHO pathways. Meanwhile, the unfavorable *CHO formation fundamentally

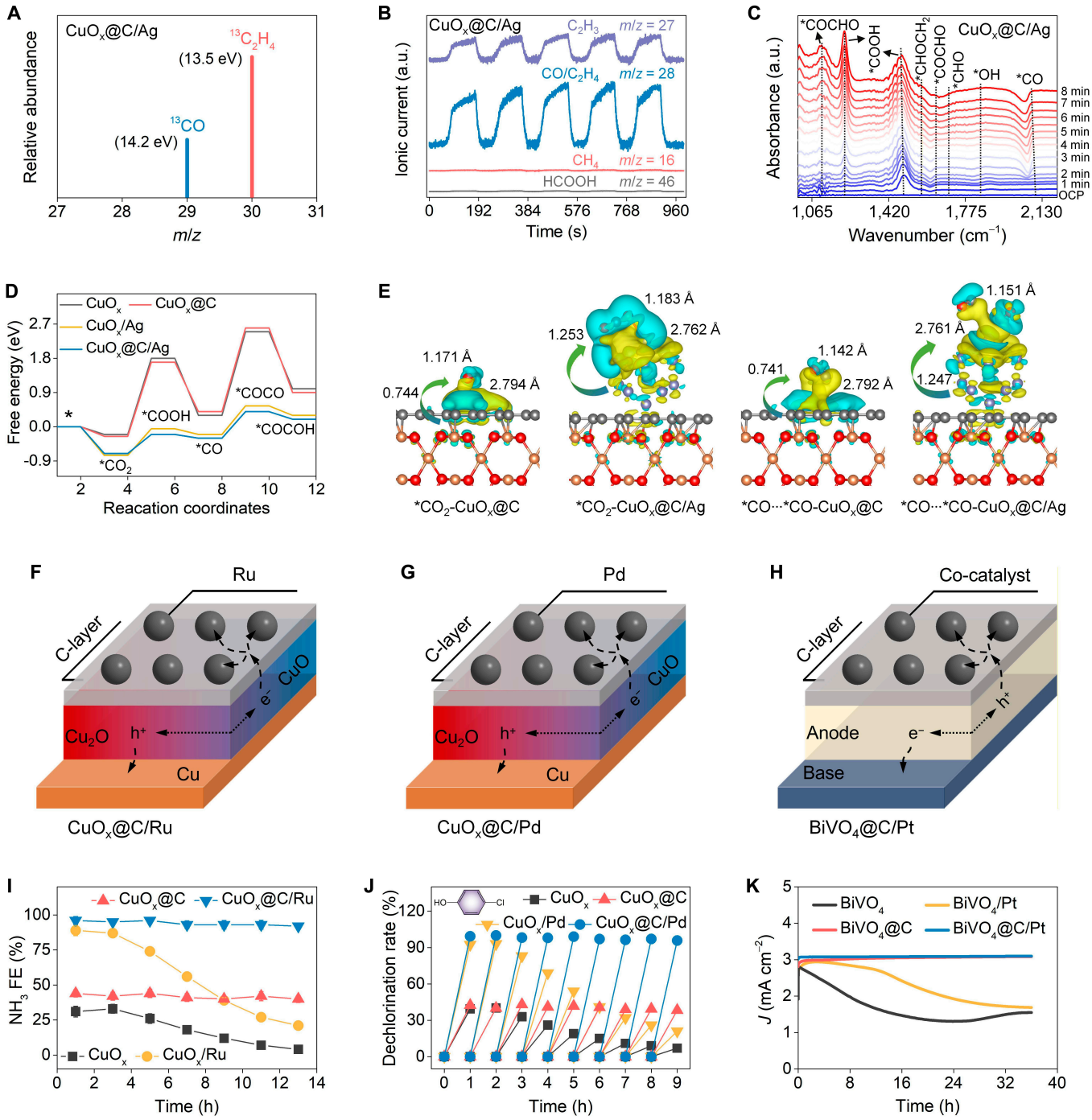


Fig. 6. Photoelectrocatalytic mechanism for CO_2-to-C_2H_4 conversion and expand applications. The (A) $^{13}CO_2$ isotopic labeling experiment, (B) differential electrochemical mass spectrometry (DEMS) analysis, and (C) insitu attenuated total reflection Fourier-transform infrared (ATR-FTIR) test for CO_2 reduction on CuO_x@C/Ag (experimental conditions: at −0.1 V vs. RHE under AM 1.5G simulated sunlight [100 mW/cm^2] using 0.1 M $KHCO_3$ as electrolyte [CO_2-saturated]). (D) The density functional theory (DFT) calculations of reaction pathways and free energy changes for CO_2 reduction on different photoelectrodes. (E) Side-view charge density difference maps between different photoelectrode bases and critical intermediates (the yellow and green regions represent net electron depletion and accumulation). Schematic diagrams of migration and separation path of photogenerated carriers in (F) CuO_x@C/Ru, (G) CuO_x@C/Pd, and (H) $BiVO_4$@C/Pt. (I) The FE of CuO_x, CuO_x@C, CuO_x/Ru, and CuO_x@C/Ru for nitrate reduction to NH_3 (experimental conditions: at −0.1V vs. RHE under AM 1.5G simulated sunlight [100 mW/cm^2] using 0.1 M Na_2SO_4 + 10 mM $NaNO_3$ as electrolyte [Ar-saturated]). (J) The rate of CuO_x, CuO_x@C, CuO_x/Pd, and CuO_x@C/Pd for dechlorination of p-chlorophenol (at −0.1V vs. RHE under AM 1.5G simulated sunlight [100 mW/cm^2] using 0.1 M Na_2SO_4 + 10 mM p-chlorophenol as electrolyte [Ar-saturated]). (K) The rate of $BiVO_4$, $BiVO_4$@C, $BiVO_4$/Pt, and $BiVO_4$@C/Pt for water oxidation (at 0.95 V vs. RHE under AM 1.5G simulated sunlight [100 mW/cm^2] using 0.1 M Na_2SO_4 as electrolyte [Ar-saturated]). Data are presented as mean ± SD (n = 3 independent chemical replicates) in (D).

explained the suppressed productions of CH_4 and CH_3OH observed experimentally. In stark contrast, CuO_x@C exhibited prohibitively high C–C coupling barrier (~2.2 eV). Further evidence emerged from the substantial charge transfer between *CO and CuO_x@C/Ag (~1.247 |e| versus ~0.741 |e| for CuO_x@C) and strengthened C–O bond activation (from 1.142 to 1.151 Å).

The complete reaction pathway on CuO_x@C/Ag for CO_2 reduction to C_2H_4 proceeded through an optimized sequence of $*CO_2 \rightarrow *COOH \rightarrow *CO \rightarrow *COCO \rightarrow *COCHO \rightarrow *COCHOH \rightarrow *CHOCHOH \rightarrow *CHOCH_2OH \rightarrow *CHOCH_2 \rightarrow *CHOHCH_2 \rightarrow *CH_2OHCH_2 \rightarrow *C_2H_4$, demonstrating how Ag incorporation simultaneously enhanced CO_2 adsorption, stabilized critical intermediates, and promoted selective C–C coupling toward C_2H_4 production.

To establish the general applicability of the coupled carbon-encapsulation and metal-decoration strategy, we further engineered a series of functional photoelectrodes, including CuO_x@C/Ru, CuO_x@C/Pd, and $BiVO_4$@C/Pt (Fig. 6F to H). These systems were respectively deployed for nitrate reduction to NH_3, chlorophenol dechlorination, and the oxygen evolution reaction, respectively (Fig. S30). A particularly noteworthy configuration was realized in the $BiVO_4$@C/Pt, where the carbon layer served as an efficient hole-extraction mediator. This led to spatial isolation of photoholes, thereby inhibiting hole-induced oxidation photocorrosion and suppressing electron–hole recombination. The FE for nitrate reduction to NH_3 on CuO_x and CuO_x/Ru sharply reduced from ~31.4% to ~4.1% and from ~89.1% to ~21.3%, respectively, after 14 h of continuous use (Fig. 6I). By contrast, CuO_x@C and CuO_x@C/Ru maintained ~95% of their initial FE for nitrate reduction to NH_3 after prolonged use. As shown in Fig. 6J, the dechlorination rate of p-chlorophenol on CuO_x and CuO_x/Pd sharply reduced from ~39.2% to ~7.4% and from ~92.3% to ~20.7%, respectively, after 9 h of continuous use. By contrast, CuO_x@C and CuO_x@C/Pd maintained ~97% of their initial dechlorination rate after prolonged use. The photocurrent densities of $BiVO_4$ and $BiVO_4$/Pt decreased over time, remaining at only ~57% of their initial values after 40 h of chronoamperometry (Fig. 6K). By contrast, $BiVO_4$@C and $BiVO_4$@C/Pt exhibited stable photocurrent during continuous operation, maintaining ~98% of their initial photocurrent density at the end of the test. It was worth mentioning that the activity and durability of CuO_x@C/Ru, CuO_x@C/Pd, and $BiVO_4$@C/Pt were outstanding and markedly superior to most existing studies (Fig. S43 and Table S1), demonstrating the synergistic carbon encapsulation and cocatalyst decoration strategy.

Conclusion

In summary, we unveiled the photoelectrochemical transformation mechanism of CuO_x during the reaction, namely, the stepwise photoelectron reduction: $Cu_2O/CuO \rightarrow Cu_2O \rightarrow Cu$. To overcome these changes, we innovatively proposed an ultrathin carbon layer encapsulation strategy formed via electrodeposition-coupled self-assembly of carbon nanodots. The synthesized CuO_x@C exhibits stable phase and photocurrent throughout prolonged operation exceeding 24 h. We then further modified CuO_x@C with different cocatalysts, including Ag, Ru, and Pd, to improve the activity and selectivity of the target reactions. The results showed that the Faraday efficiencies for CO_2 reduction to C_2H_4 on CuO_x@C/Ag, nitrate reduction to NH_3 on CuO_x@C/Ru, and dechlorination of p-chlorophenol on CuO_x@C/Pd were as high as ~66.4%, ~97.5%, and ~99.2%, respectively, with each maintaining >95% of its initial performance after prolonged use. Additionally, this protection approach was successfully extended beyond CuO_x to other photoelectrodes, such as $BiVO_4$. This work provides insights into investigating the chemical alterations in metal oxides under reaction conditions and opens new avenues for the rational design of efficient and durable photoelectrocatalytic materials to realize sustainable energy conversion and environmental purification.

Materials and Methods

Information about the materials and methods used in this work is provided in the Supplementary Materials.

Acknowledgments

Funding: This work is financially supported by the National Natural Science Foundation of China (52300096 and 52570024) and the Talent Startup Fund of Beijing Normal University (312200502507 and 312225502403).

Author contributions: S.Q. and J.Z. conceived the idea and designed the experiments. S.Q., J.Z., and R.Y. implemented the experimental setup and conducted the experiments. S.Q., M.G., and R.Y. carried out the DFT calculations. S.Q. and J.Z. wrote the manuscript. J.Z. supervised the work. All the authors discussed the results and commented on the manuscript.

Competing interests: The authors declare that they have no competing interests.

Data Availability

The data that support the findings of this study are available from the corresponding author upon reasonable request.

Supplementary Materials

Supplementary Methods
Figs. S1 to S45
Table S1

References

1. Shindell D, Smith CJ. Climate and air-quality benefits of a realistic phase-out of fossil fuels. *Nature*. 2019;573(7774):408–441.
2. Wu Y, Jiang Z, Lu X, Liang Y, Wang H. Domino electroreduction of CO_2 to methanol on a molecular catalyst. *Nature*. 2019;575:639–642.
3. Zhu P, Wu ZY, Elgazzar A, Dong C, Wi TU, Chen FY, Xia Y, Feng Y, Shakouri M, Kim JY, et al. Continuous carbon capture in an electrochemical solid-electrolyte reactor. *Nature*. 2023;618(7967):959–966.
4. Liu G, Zheng F, Li J, Zeng G, Ye Y, Larson DM, Yano J, Crumlin EJ, Ager JW, Wang LW, et al. Investigation and mitigation of degradation mechanisms in Cu_2O photoelectrodes for CO_2 reduction to ethylene. *Nat Energy*. 2021;6:1124–1132.
5. Bhattacharjee S, Rahaman M, Andrei V, Miller M, Rodríguez-Jiménez S, Lam E, Pornrungroj C, Reisner E. Photoelectrochemical CO_2-to-fuel conversion with simultaneous plastic reforming. *Nat Synth*. 2023;2:182–192.
6. Sendeku MG, Shifa TA, Dajan FT, Ibrahim KB, Wu B, Yang Y, Moretti E, Vomiero A, Wang F. Frontiers in photoelectrochemical catalysis: A focus on valuable product synthesis. *Adv Mater*. 2024;36(21):Article e2308101.
7. Schreier M, Luo J, Gao P, Moehl T, Mayer MT, Grätzel M. Covalent immobilization of a molecular catalyst on

Cu_2O photocathodes for CO_2 reduction. *J Am Chem Soc*. 2016;138(6):1938–1946.
8. He T, Zhao Y, Benetti D, Moss B, Tian L, Selim S, Li R, Fan F, Li Q, Wang X, et al. Facet-engineered $BiVO_4$ photocatalysts for water oxidation: Lifetime gain versus energetic loss. *J Am Chem Soc*. 2024;146(39):27080–27089.
9. Zhou X, Fu B, Li L, Tian Z, Xu X, Wu Z, Yang J, Zhang Z. Hydrogen-substituted graphdiyne encapsulated cuprous oxide photocathode for efficient and stable photoelectrochemical water reduction. *Nat Commun*. 2022;13(1):5770.
10. Zhang Y, Lv H, Zhang Z, Wang L, Wu X, Xu H. Stable unbiased photo-electrochemical overall water splitting exceeding 3% efficiency via covalent triazine framework/metal oxide hybrid photoelectrodes. *Adv Mater*. 2021;33(15):Article e2008264.
11. Pan L, Dai L, Burton OJ, Chen L, Andrei V, Zhang Y, Ren D, Cheng J, Wu L, Frohna K, et al. High carrier mobility along the [111] orientation in Cu_2O photoelectrodes. *Nature*. 2024;628(8009):765–770.
12. Yoon A, Bai L, Yang F, Franco F, Zhan C, Rüscher M, Timoshenko J, Pratsch C, Werner S, Jeon HS, et al. Revealing catalyst restructuring and composition during nitrate electroreduction through correlated operando microscopy and spectroscopy. *Nat Mater*. 2025;24:762–769.
13. Kim HE, Wi DH, Lee JS, Choi K-S. Photoelectrochemical nitrate and nitrite reduction using Cu_2O photocathodes. *ACS Energy Lett*. 2024;9(5):1993–1999.
14. Wu H, Kong XY, Wen X, Chai SP, Lovell EC, Tang J, Ng YH. Metal-organic framework decorated cuprous oxide nanowires for long-lived charges applied in selective photocatalytic CO_2 reduction to CH_4. *Angew Chem Int Ed Engl*. 2021;60(15):8455–8459.
15. Tan J, Kang B, Kim K, Kang D, Lee H, Ma S, Jang G, Lee H, Moon J. Hydrogel protection strategy to stabilize water-splitting photoelectrodes. *Nat Energy*. 2022;7:537–547.
16. Liu Y, Tan H, Wei Y, Liu M, Hong J, Gao W, Zhao S, Zhang S, Guo S. Cu_2O/2D COFs core/shell nanocubes with antiphotocorrosion ability for efficient photocatalytic hydrogen evolution. *ACS Nano*. 2023;17(6):5994–6001.
17. Yang Y, Ling Y, Wang G, Liu T, Wang F, Zhai T, Tong Y, Li Y. Photohole induced corrosion of titanium dioxide: Mechanism and solutions. *Nano Lett*. 2015;15(10):7051–7057.
18. Yang JW, Ji SG, Jeong CS, Kim J, Kwon HR, Lee TH, Lee SA, Cheon WS, Lee S, Lee H, et al. High-efficiency unbiased water splitting with photoanodes harnessing polycarbazole hole transport layers. *Energy Environ Sci*. 2024;17(7):2541–2553.
19. Huang W, Luo W, Liu J, Jia BE, Lee C, Dong J, Yang L, Liu B, Yan Q. Cascade electrocatalytic nitrate reduction reaching 100% nitrate-N to ammonia-N conversion over Cu_2O@CoO yolk-shell nanocubes. *ACS Nano*. 2024;18(31):20258–20267.
20. Wang Z, Liu D, Xia C, Shi X, Zhou Y, Liu Q, Huang J, Wu H, Zhu D, Zhang S, et al. Tip carbon encapsulation customizes cationic enrichment and valence stabilization for low K^+ acidic CO_2 electroreduction. *Nat Commun*. 2025;16:1754.
21. Li C, Hisatomi T, Watanabe O, Nakabayashi M, Shibata N, Domen K, Delaunay JJ. Positive onset potential and stability of Cu_2O-based photocathodes in water splitting by atomic layer deposition of a Ga_2O_3 buffer layer. *Energy Environ Sci*. 2015;8(5):1493–1500.
22. Lange T, Reichenberger S, Rohe M, Bartsch M, Kampermann L, Klein J, Strunk J, Bacher G, Schlögl R, Barcikowski S. Alumina-protected, durable and photostable zinc sulfide particles from scalable atomic layer deposition. *Adv Funct Mater*. 2021;31(14):2009323.
23. Tian Z, Zhang P, Qin P, Sun D, Zhang S, Guo X, Zhao W, Zhao D, Huang F. Novel black $BiVO_4/TiO_{2-x}$ photoanode with enhanced photon absorption and charge separation for efficient and stable solar water splitting. *Adv Energy Mater*. 2019;9(27):1901287.
24. Cui L, Zhao X, Xie H, Zhang Z. Overcoming the activity-stability trade-off in heterogeneous electro-Fenton catalysis: Encapsulating carbon cloth-supported iron oxychloride within graphitic layers. *ACS Catal*. 2022;12(21):13334–13348.
25. He J, Bhargav A, Manthiram A. Covalent organic framework as an efficient protection layer for a stable lithium-metal anode. *Angew Chem Int Ed Engl*. 2022;61(18):Article e202116586.
26. Li B, Ma J-G, Cheng P. Silica-protection-assisted encapsulation of Cu_2O nanocubes into a metal-organic framework(ZIF-8) to provide a composite catalyst. *Angew Chem Int Ed Engl*. 2018;57(23):6834–6837.
27. Dong H, Luo R, Zhang G, Li L, Wang C, Sun G, Wang H, Liu J, Wang T, Zhao ZJ, et al. Electrochemical epoxidation enhanced by CH activation and hydroxyl generation at the Ag/SnO interface. *Nat Commun*. 2025;16:1901.
28. Chen F-Y, Wu ZY, Gupta S, Rivera DJ, Lambeets SV, Pecaut S, Kim JYT, Zhu P, Finfrock YZ, Meira DM, et al. Efficient conversion of low-concentration nitrate sources into ammonia on a Ru-dispersed Cu nanowire electrocatalyst. *Nat Nanotechnol*. 2022;17:759–767.
29. Li Z, Guo Z, Wu X, Jiang X, Li H, Xu J, Yang K, Lin D. Few-atomic zero-valent palladium ensembles for efficient reductive dehydrogenation and dehalogenation catalysis. *ACS Nano*. 2023;17(22):22859–22871.
30. Zhang J, Ji Q, Lan H, Zhang G, Liu H, Qu J. Synchronous reduction-oxidation process for efficient removal of trichloroacetic acid: H* initiates dechlorination and •OH is responsible for removal efficiency. *Environ Sci Technol*. 2019;53(24):14586–14594.
31. Zhang J, Ma Y, du Y, Jiang H, Zhou D, Dong S. Carbon nanodots/WO_3 nanorods Z-scheme composites: Remarkably enhanced photocatalytic performance under broad spectrum. *Appl Catal B Environ Energy*. 2017;209:253–264.
32. Zhang J, Zhang G, Ji Q, Lan H, Qu J, Liu H. Carbon nanodot-modified FeOCl for photo-assisted Fenton reaction featuring synergistic in-situ H_2O_2 production and activation. *Appl Catal B Environ Energy*. 2020;266:Article 118665.
33. Deng X, Zhang J, Qi K, Liang G, Xu F, Yu J. Ultrafast electron transfer at the In_2O_3/Nb_2O_5 S-scheme interface for CO_2 photoreduction. *Nat Commun*. 2024;15(1):4807.
34. Meng K, Zhang J, Cheng B, Ren X, Xia Z, Xu F, Zhang L, Yu J. Plasmonic near-infrared-response S-scheme ZnO/$CuInS_2$ photocatalyst for H_2O_2 production coupled with glycerin oxidation. *Adv Mater*. 2024;36(32):2406460.
35. Sun F, Deng Y, Leng J, Shi M, Li C, Jin S, Li R, Tian W. Visualizing ultrafast photogenerated electron and hole separation in facet-engineered bismuth vanadate crystals. *J Am Chem Soc*. 2024;146(45):31106–31113.
36. Chen R, Ren Z, Liang Y, Zhang G, Dittrich T, Liu R, Liu Y, Zhao Y, Pang S, An H, et al. Spatiotemporal imaging of charge transfer in photocatalyst particles. *Nature*. 2022;610:296–301.
37. Mao J, An X, Gu Z, Zhou J, Liu H, Qu J. Visualizing the interfacial charge transfer between photoactive microcystis aeruginosa and hydrogenated TiO_2. *Environ Sci Technol*. 2020;54(16):10323–10332.

38. Bai L, Franco F, Timoshenko J, Rettenmaier C, Scholten F, Jeon HS, Yoon A, Rüscher M, Herzog A, Haase FT, et al. Electrocatalytic nitrate and nitrite reduction toward ammonia using Cu_2O nanocubes: Active species and reaction mechanisms. *J Am Chem Soc*. 2024;146(14):9665–9678.
39. Liu W, Zhai P, Li A, Wei B, Si K, Wei Y, Wang X, Zhu G, Chen Q, Gu X, et al. Electrochemical CO_2 reduction to ethylene by ultrathin CuO nanoplate arrays. *Nat Commun*. 2022;13(1):1877.
40. Costa GF, Winkler M, Mariano T, Pinto MR, Messias I, Souza JB Jr, Neckel IT, Santos MFC, Tormena CF, Singh N, et al. Identifying the active site of cu/Cu_2O for electrocatalytic nitrate reduction reaction to ammonia. *Chem Catal*. 2024;4(1):Article 100850.
41. Xu T, Yang H, Lu T, Zhong R, Lv JJ, Zhu S, Zhang M, Wang ZJ, Yuan Y, Li J, et al. Microenvironment engineering by targeted delivery of Ag nanoparticles for boosting electrocatalytic CO_2 reduction reaction. *Nat Commun*. 2025;16(1):977.
42. Chen CB, Li Y, Yu S, Louisia S, Jin J, Li M, Ross MB, Yang P. Cu-Ag tandem catalysts for high-rate CO_2 electrolysis toward multicarbons. *Joule*. 2020;4(8):1688–1699.
43. Liu SC, Zhou Q, Wen D, Wu C, Pan Y, Liu X, Huang Z, Li N. Particle size-dependent charge transfer dynamics for boosting CO_2 photoreduction over ag/TiO_2 heterojunction. *ACS Catal*. 2024;14(10):8105–8115.
44. Kim J, Lee T, Jung HD, Kim M, Eo J, Kang B, Jung H, Park J, Bae D, Lee Y, et al. Vitamin C-induced CO_2 capture enables high-rate ethylene production in CO_2 electroreduction. *Nat Commun*. 2024;15(1):192.
45. Chen Y, Fan Z, Wang J, Ling C, Niu W, Huang Z, Liu G, Chen B, Lai Z, Liu X, et al. Ethylene selectivity in electrocatalytic CO_2 reduction on Cu nanomaterials: A crystal phase-dependent study. *J Am Chem Soc*. 2020;142(29): 12760–12766.
46. Bai SJ, Jing W, He G, Liao C, Wang F, Liu Y, Guo L. Near-infrared-responsive photocatalytic CO_2 conversion via in-situ generated Co_3O_4/Cu_2O. *ACS Nano*. 2023;17(11):10976–10986.
47. van den Berg D, Lopuhaä HP, Kortlever R. Direct quantification of electrochemical CO_2 reduction products with an improved DEMS setup. *Chem Catal.* 2024;4(8): Article 101065.
48. Yao Y, Shi T, Chen W, Wu J, Fan Y, Liu Y, Cao L, Chen Z. A surface strategy boosting the ethylene selectivity for CO_2 reduction and in situ mechanistic insights. *Nat Commun*. 2024;15(1):1257.
49. Wang S, Li F, Zhao J, Zeng Y, Li Y, Lin ZY, Lee TJ, Liu S, Ren X, Wang W, et al. Manipulating C-C coupling pathway in electrochemical CO_2 reduction for selective ethylene and ethanol production over single-atom alloy catalyst. *Nat Commun*. 2024;15:10247.